A damage mechanics approach for lifetime estimation of wind turbine gearbox materials

Jantara Junior, Valter Luiz; Basoalto, Hector; Papaelias, Mayorkinos

DOI:
10.1016/j.ijfatigue.2020.105671

Document Version
Peer reviewed version

Citation for published version (Harvard):
Jantara Junior, VL, Basoalto, H & Papaelias, M 2020, 'A damage mechanics approach for lifetime estimation of wind turbine gearbox materials', *International Journal of Fatigue*, vol. 137, 105671.
https://doi.org/10.1016/j.ijfatigue.2020.105671

A damage mechanics approach for lifetime estimation of wind turbine gearbox materials

Valter Luiz Jantara Junior[a,*], Hector Basoalto[a], Mayorkinos Papaelias[a]

[a]*School of Metallurgy and Materials, University of Birmingham, Birmingham, UK*

Abstract

Wind turbine gearboxes (WTG) have been suffering from premature failures and rarely live up to their designed lifetime. This study focuses on a better understanding of WTG failures. A finite element model of a gear pair was coupled with a constitutive model to quantify and predict damage, while also testing for different service conditions. A damage mechanics formulation is presented based on a physics-based dislocation slip model. Additionally, an estimation of the remaining useful lifetime of the component was generated, further assisting wind turbine farm operators to move towards the implementation of a truly predictive maintenance approach.

Keywords: Wind turbine gearbox, damage, lifetime estimation, constitutive model

2010 MSC: 74A45, 74C10

1. Introduction

Wind power plays a major role amongst utility-scale renewable energy power generation, experiencing an average annual growth rate of 23% over the last decade. The total global installed capacity has reached 591 GW as of 2017 contributing more than 5% of the total global electricity demand [1]. At the same time, the rated power capacity of wind turbines has greatly increased from 15 kW in the 1980s to around 10 MW in 2018 [2], whilst 12 MW models are being

*Corresponding author

Email address: v.l.jantarajunior@bham.ac.uk (Valter Luiz Jantara Junior)

designed [3]. To enable the production of higher power output, the diameter of the rotor has increased as well, reaching lengths up to 164 m. Historical trends imply that power capacity and size of wind turbines will keep increasing with 20 MW models being quite possible in the mid-term future [4]. However, the expansion of wind power capacity has been restricted due to a number of operational challenges which are yet to be addressed. The most important of these challenges appear to be the reliability of the wind turbine gearbox (WTG). WTGs are currently unable to survive their predicted design lifetime of 20-25 years. Most of them hardly reach a useful operational lifetime of more than 7 years without serious refurbishment or replacement. In offshore wind turbines, failure occurs even earlier due to the highly variable loads experienced, resulting in rapid structural degradation. Early and unexpected gearbox failures can result in additional expenditure due to the loss of production as well as associated corrective maintenance costs. Gearbox failures can be related to gear, bearing, or shaft failures. In the United Kingdom, it is estimated that 20% of the Levelised Cost of Electricity (LCOE) produced by offshore wind farms arises due to operation and repairs [5].

Figure 1 shows different damage mechanisms in the same tooth retrieved from an industrial wind turbine including overheating, plastic flow, and scuffing.

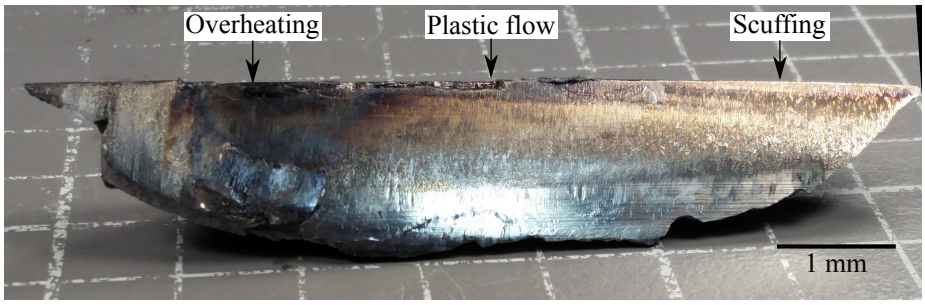

Figure 1: Broken gear tooth retrieved from the intermediate stage of an industrial wind turbine showing different damage mechanisms.

There are different ways to approach the modelling of plastic flow of a material. One of the options is to use an empirical model. Several examples of

these are given in ref. [6]. For example, the power law shown on equation (1) has been extensively used for modelling creep [7].

$$\dot{\varepsilon} = A\ \sigma^n \tag{1}$$

Another option is to use a Chaboche style model [8], as was done by Bernhart et al. [9] for modelling the behaviour of a martensitic forging tool steel on high temperature low cycle fatigue. These models take into account both isotropic and kinematic hardening effects. However, extrapolation of these models is not always straight-forward and care must be taken in the parametrisation of its variables.

Yet another option is to employ a microstructure-based physical model. These models explicitly link the microstructure of the material to its deformation behaviour. By capturing the physical mechanism driving deformation, these models allow for better extrapolation and prediction of properties. The main challenge associated with this approach is mathematically describing the physical mechanisms in a general and easy to implement way, predicting the behaviour rather than having it hardwired into the model. Examples of this type of model can be found in refs. [10] and [11].

Previous numerical investigations have modelled damage initiation and accumulation in gears or other components that are subjected to rolling contact fatigue. Pandkar et al. [12] studied the contribution of hard particles in bearing steels subjected to rolling contact fatigue. A non-linear model with isotropic and kinematic hardening was used. They concluded that the particles, acting as stress concentrators, introduce shear stresses which generates ratcheting in the metal matrix. Other heterogeneities, such as pores, inclusions and dislocations might also generate the same effect. Osman and Velex [13] created a model that takes into account the influence of dynamic loading conditions on pitting formation on gears. The dynamic loads were found to influence damage depending on the speed range, with higher speeds being more detrimental than lower speeds. It was also found that the tip relief on both gears and pinions are

an important factor in reducing the fatigue damage in the engagement area.

Franulovic et al. [14] used a non-linear kinematic hardening model in order to predict low-cycle fatigue in the tooth root of gears due to short-time overloads. The model combines isotropic and kinematic hardening with damage mechanics to simulate damage nucleation and initiation. Even though a good agreement was found, the model lacks the ability to predict other types of damage, such as rolling contact fatigue, and, more importantly, any type of damage that develops after the low-cycle fatigue stage. Brandão et al. [15, 16] used a numerical model to predict micropitting and mass loss of a spur gear. The model is dependant on roughness data, which was obtained from FZG tests (a rig where one gear is loaded against another by an electric motor). The model showed an accurate prediction of the mass loss of the gear, however, the predicted roughness evolution did not correlate well with the laboratory tests.

The objective of this paper is to develop a constitutive description for the predictions of damage initiation and accumulation in steel gears under different service condition situations. This paper focuses on the rolling contact fatigue failure mechanism (RCF), which generates a complex triaxial stress state at the subsurface of the mating surfaces of gear teeth. The proposed constitutive model is a state variable approach to plasticity based on dislocation slip within grains. It accounts for the evolution of the mobile dislocation density through a continuity condition, which is then used to calculate the plastic strain rate. Redistribution of stresses between plastically hard and soft domains are taken into account and give rise to kinematic back stresses. Dislocation elastic reactions are accounted by a simple strength model that is associated with isotropic hardening. The resulting constitutive description has been implemented within a commercial finite element software through user-subroutines.

2. Modelling Framework

2.1. Deformation kinematics

Consider the deformation of a material domain from an initial configuration to the current state. The mapping between the states is achieved through the deformation gradient tensor $\boldsymbol{F}$. Decomposition of the total deformation gradient into elastic $\boldsymbol{F}^e$ and plastic $\boldsymbol{F}^p$ contributions is expressed as the multiplicative rule [17]

$$\boldsymbol{F} = \boldsymbol{F}^e \boldsymbol{F}^p \tag{2}$$

The rate at which neighbouring points are being displaced is described by the velocity gradient tensor

$$\boldsymbol{L} = \boldsymbol{F}\dot{\boldsymbol{F}}^{-1} \tag{3}$$

and the insertion of equation (2) in it results in

$$\boldsymbol{L} = \dot{\boldsymbol{F}}^e \boldsymbol{F}^{e-1} + \boldsymbol{F}^{e-1}\dot{\boldsymbol{F}}^p \boldsymbol{F}^{p-1}\boldsymbol{F}^e \tag{4}$$

The velocity gradient tensor is further decomposed into symmetric and anti-symmetric parts, which correspond to the stretch $\boldsymbol{D}$ and spin tensors $\boldsymbol{W}$, respectively. These are given by

$$\boldsymbol{D} = \mathrm{sym}(\boldsymbol{L}) = \frac{1}{2}\left(\boldsymbol{L} + \boldsymbol{L}^T\right) \tag{5}$$

$$\boldsymbol{W} = \mathrm{asym}(\boldsymbol{L}) = \frac{1}{2}\left(\boldsymbol{L} - \boldsymbol{L}^T\right) \tag{6}$$

The total stretch and spin tensors can be further decomposed into elastic and plastic contributions

$$\boldsymbol{D} = \boldsymbol{D}^e + \boldsymbol{D}^p \tag{7}$$

$$\boldsymbol{W} = \boldsymbol{W}^e + \boldsymbol{W}^p \tag{8}$$

Assuming J_2-plasticity theory, the plastic stretch can be calculated from the following relation

$$\boldsymbol{D}^p = \frac{3}{2}\frac{\dot{\varepsilon^p}}{\overline{\sigma}}\boldsymbol{S} \tag{9}$$

where $\dot{\varepsilon^p}$ is the plastic strain rate, $\overline{\sigma}$ is the equivalent stress, and $\boldsymbol{S}$ is the deviatoric stress tensor. The plastic strain rate will be obtained in the following section with the use of a constitutive equation.

The Jaumann rate of the stress tensor is

$$\overset{\triangledown}{\boldsymbol{\sigma}} = \boldsymbol{C}\,(\boldsymbol{D} - \boldsymbol{D}^p) \tag{10}$$

where $\boldsymbol{C}$ is the fourth-order tensor of material constants. The Cauchy, $\dot{\boldsymbol{\sigma}}$, and Jaumman stress rates are related through the total spins according to the relation

$$\overset{\triangledown}{\boldsymbol{\sigma}} = \dot{\boldsymbol{\sigma}} - \boldsymbol{W}.\boldsymbol{\sigma} + \boldsymbol{\sigma}.\boldsymbol{W} \tag{11}$$

2.2. Constitutive model

This section focuses on the derivation of a constitutive description for gear steel materials subject to cyclic loading conditions. Deformation proceeds by the movement of dislocations, where slip events result in plastic deformation. The plastic deformation rate will scale linearly with the dislocation flux, which is the product of the mobile dislocation density ρ and mean their mean gliding velocity v_g. This flux can be estimated from a continuity condition of the mobile dislocation density. In this model the rate of change of mobile dislocation segments $\dot{\rho}$ is governed by the difference between generation $\dot{\rho}^+$ and annihilation rates $\dot{\rho}^-$ for the mobile dislocations population, i.e., $\dot{\rho} = \dot{\rho}^+ - \dot{\rho}^-$. For the annihilation rate it will be assumed that all gliding segments will form dislocation dipoles at a frequency v_g/λ_m, where λ_m is the mean free path. Following Kocks *et al*. [18] the dipole mean free path is given by $\lambda_m = MGb_v/[4(1-\nu)\rho\bar{\sigma}]$, where $\bar{\sigma}$ is the effective stress, G is the shear modulus, b_v the Burgers vector, M is the Taylor factor and ν is Poisson's ratio. Suppose that there is a density ρ_s of dislocation sources which are emitted at a frequency $\Gamma^+(\bar{\sigma}, T)$, where T is the temperature. It follows that the continuity condition for the mobile scalar dislocation density may be expressed as

$$\dot{\rho} = \rho_s\ \Gamma^+(\bar{\sigma}, T) - \rho^2 \frac{4(1-\nu)\bar{\sigma}}{MGb_v} \tag{12}$$

In the present work it will be assumed that ρ_s and $\Gamma^+(\bar{\sigma}, T) = v_g(\bar{\sigma}, T)/l$ are governed by the dislocation network, so that $\rho_s = \rho$ and $1/\sqrt{\rho}$.

An expression for the shear rate will now be derived. It will be assumed that dislocation movement on active slip systems will exhibit a jerky behaviour. Physically this is associated with the pinning and release of the dislocation line segments. Suppose that the mean area rate swept out by dislocation segments as a result of a release event be $\dot{A}_s$ then the shear rate $\dot{\gamma}$ is given by $\dot{\gamma} = b_v \ \dot{A}_s/V$, where b_v is the magnitude of the Burgers vector and V the volume of the deforming domain. Consider a dislocation line on some active slip system. Let the mean pinning spacing be λ_p. Then the number of pinning points on per unit length of the dislocation line is approximately $1/\lambda_p$. If $P[r|w]$ is the probability of a waiting segment being released and ν_e be the escape frequency then the number of escape events is estimated to be $\nu_e \ P[r|g] \ /\lambda_p$. Approximating the slipped area and taking $A_s \approx L \ \lambda_p$, where L is the total length of mobile dislocations, then the following expression for the slip area rate $\dot{A}_s = A_s \ \nu_e \ P[r|g]/\lambda_p = L \ \nu_e \ P[r|g]$. For the probability of release, it will be assumed $P[r|g] = p_0 \ exp(-\delta F/kT) exp(\tau b_v \lambda_p/kT)$, where δF is an activation energy for the process, k is Boltzmann's constant and T the temperature. It will be further assumed that the macroscale plastic strain rate $\dot{\epsilon}^p$ will have the same form as the shear strain rate on an active slip system, so that $\dot{\epsilon}^p = \dot{\gamma}/M$. From these considerations the shear strain rate on an active slip system will have the form

$$\dot{\epsilon}^p = \dot{\epsilon}_0 \ \rho \ exp(-Q_{d,j}/RT) exp(\bar{\sigma} b_v \lambda_p/MkT) \tag{13}$$

where $\dot{\epsilon}_0 = \nu_e \ p_0$, $\bar{\sigma} = M \ \tau$, $\rho = L/V$, $Q_{d,j} = \delta F N_a$, N_a is Avogrado's number and R is the Universal gas constant.

In this study the pinning points may be associated with dislocation reactions (formation of dislocation junctions as well as kinks, jogs) and pinning by hard particles (such as carbides). To account for these different mechanisms the pinning distance will be approximated by a root mean square addition given by $\lambda_p^2 = \lambda_{or}^2 + \rho_m$, where $\lambda_{or} = Gb/\sigma^{or}$ is a spacing associated with Orowan

by-pass hard pinning particles (with an Orowan stress σ^{or}) and the second term is associated with the dislocation link length ($1/\sqrt{\rho_m}$). Dislocation interactions leading to dipole formation results in bundles or walls of dislocations. In the cell walls, the dislocations are tangled and their density is high, resulting in a heterogeneous distribution of dislocations within localised hard regions. Deformation between grains will not be the same and will result in an addition non-homogeneous distribution of plastic strains. Compatibility requirements will result in redistribution of stress between plastically soft and hard regions and give rise to a backstress (σ^{ks}). The evolution of such a back stress will be assume to follow that proposed by Basoalto and Dyson [19], where for small plastic strains σ^{ks} scales linearly with $\dot{\epsilon}^p$ and saturates as deformation proceeds to a value given by $H^*\bar{\sigma}$. The development of such a kinematic back stress will modify the stress driving plastic flow. The effective stress will be taken to be $\bar{\sigma} - \sigma^{ks}$. Furthermore, the evolution of damage will influence the effective stress. This will be taken into account by the introduction of a damage variable ψ, which represents the reduction of load bearing area, such that $\psi = 0$ when there is no damage (no cavities) and $\psi = 1$ corresponds to a fully cavitated area. In this case the effective stress becomes $(\bar{\sigma} - \sigma^{ks})/\psi$.

The model equations used are given by the following set of constitutive

equations

$$\dot{\epsilon^p} = C^1 \ \rho \ exp\left(\frac{\overline{\sigma} - \sigma^{ks}}{\sigma^{is}(1-\psi)}\right) \tag{14}$$

$$\dot{\sigma}^{ks} = h^s \left(1 - \frac{\sigma^{ks}}{H^* \ \overline{\sigma}}\right) \dot{\epsilon^p} \tag{15}$$

$$\dot{\rho} = C^2 \ \sqrt{\rho} \left(1 - \sqrt{\frac{\rho}{\rho^{ss}}}\right) \dot{\epsilon^p} \tag{16}$$

$$\dot{\psi} = \left(\frac{k^D}{(1-\psi)}\right) \dot{\epsilon^p} \tag{17}$$

$$\rho^{ss} = \left[C^3 \left(\frac{\overline{\sigma} - \sigma^{ks}}{1-\psi}\right)\right]^2 \tag{18}$$

$$\sigma^{is} = \sqrt{(\sigma^p)^2 + C^4 \ \rho} \tag{19}$$

$$\sigma^p = \frac{MkT\sigma^{or}}{Gb_v^3} \tag{20}$$

$$C^1 = \dot{\epsilon}_0 \ exp\left(\frac{-Q_{d,j}}{RT}\right) \tag{21}$$

$$C^2 = \frac{M}{b_v \beta} \tag{22}$$

$$C^3 = \frac{2\pi}{b_v \beta GM} \tag{23}$$

$$C^4 = \left(\frac{kT}{b_v^2}\right)^2 \tag{24}$$

A Kachanov-Rabotnov approach for the damage is used, combining Rabotnov's [20] concept of effective stress with Kachanov's [21] definition of damage. Due to the accumulation of damage, the stiffness of the material is degraded following the rule:

$$E_\psi = E(1-\psi) \tag{25}$$

where E and E_ψ the Young's modulus of the undamaged and damaged material, respectively. In order to achieve a stable solution, the Newton-Raphson implicit integration technique was implemented in this work.

2.3. Finite element implementation

The commercial finite element software ABAQUS was used to draw two spur gears. Its parameters can be found in Table 1.

Table 1: Gear pair specification.

Gear parameter	**Value**	**Unit**
Module	2	mm
Number of teeth of the pinion	34	-
Number of teeth of the gear	34	-
Pitch radius of the pinion	68	mm
Pitch radius of the gear	68	mm
Face width	20	mm
Pressure angle	20	°
Addendum	2	mm
Dedendum	2.5	mm
Tooth height	4.5	mm
Root fillet radius	0.6	mm
Clearance	0.5	mm
Tip relief	0.25	mm

The gears were then brought into contact. A contact interaction between gears was defined as "hard contact" normal behaviour, along with a "penalty" tangential behaviour, with the friction coefficient varying depending on the analysis. A surface-to-surface contact was then created with "finite sliding" for each tooth pair, totalling 34 interactions. Coupling constraints were used to simulate shafts, with reference points created on the centre of each gear. The boundary conditions were then applied at these reference points. Both gears were restrained in all directions, except the rotational direction in the z-axis (UR3). Then, an angular velocity of 157.08 rad/s was applied instantaneously to the one gear while the torque was applied to the other. This velocity is equivalent to the 1500 rpm that the gears in the high-speed shaft of a WTG are subjected to. Both gears were meshed with C3D8 elements, with a finer mesh in the flanks of the gears, as shown in Figure 2.

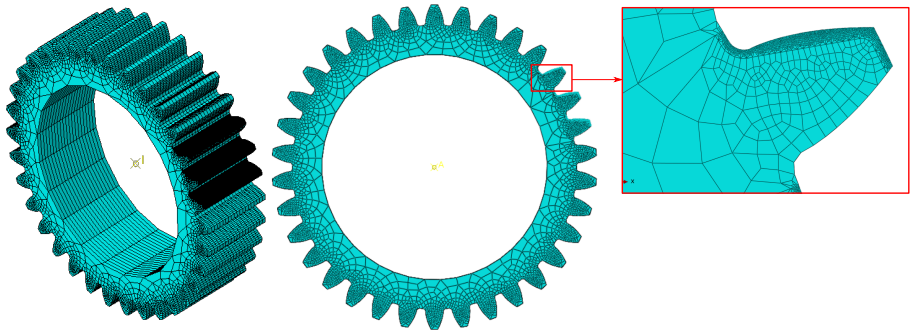

Figure 2: Mesh generated on one of the gears, showing the coarse mesh on the majority of the gear (left) and fine mesh on one of the partitioned teeth (right).

A mesh convergence analysis was performed and convergence was achieved at 120,000 elements, as can be seen in Figure 3. Elastic solutions for the finite element model were compared with the the American Gear Manufacturers Association (AGMA) fundamental stress equations [22], for both bending stress and contact stress. The comparison between the finite element analysis (FEA) and AGMA is shown in Figure 4. A good agreement can be seen, especially for the contact stresses.

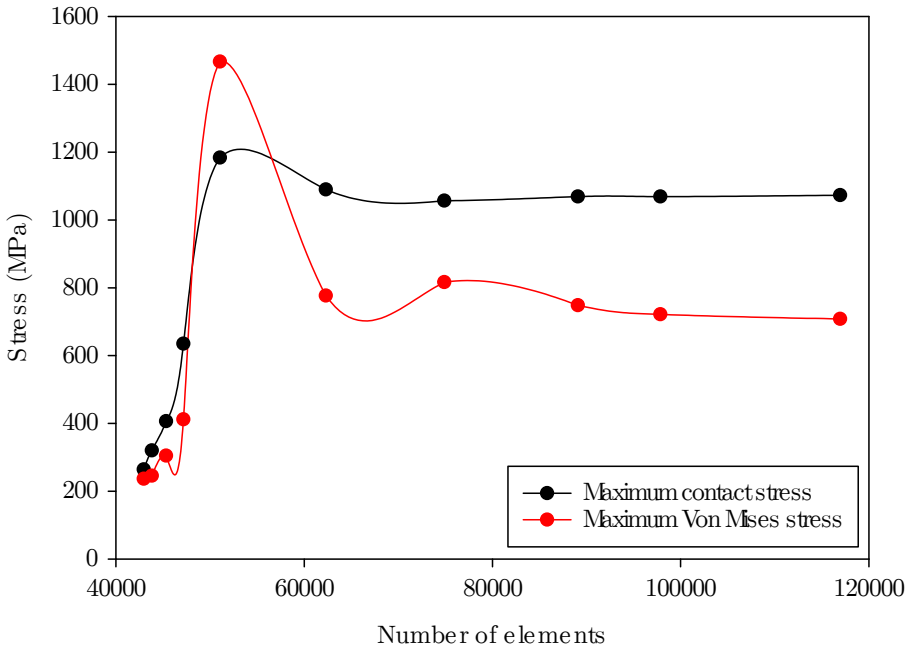

Figure 3: Mesh convergence analysis for maximum contact and maximum Von Mises stress.

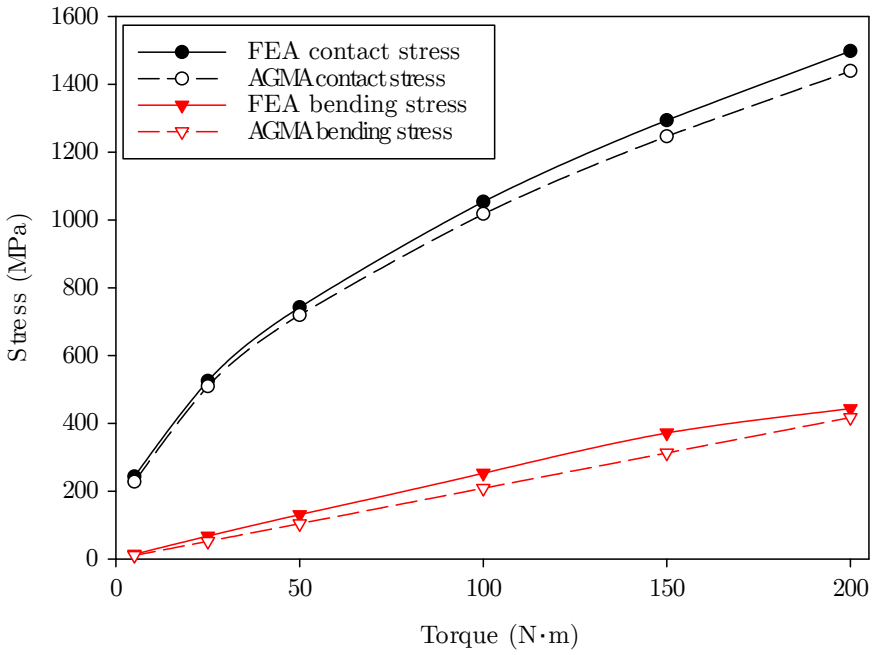

Figure 4: Comparison between FEA results and AGMA calculations on the contact and bending stresses.

2.4. Numerical implementation

The constitutive framework outlined in the previous section has been implemented within the commercial finite element software ABAQUS [23]. This was achieved through the development of a material user-defined subroutine (UMAT). In order to identify the model parameters, the UMAT was used in uniaxial tensile simulations. The results obtained were then then compared and calibrated to the results of the EN24T steel (Figure 5), commonly used in gear manufacturing. A good agreement was obtained. The material in the model was deemed as failed when the damage variable reached a value of 0.5. Such value makes the failure strain of the simulation to match that of experiment. The results were not corrected for necking, as they should not change significantly. The values for the parameters are shown in Table 2.

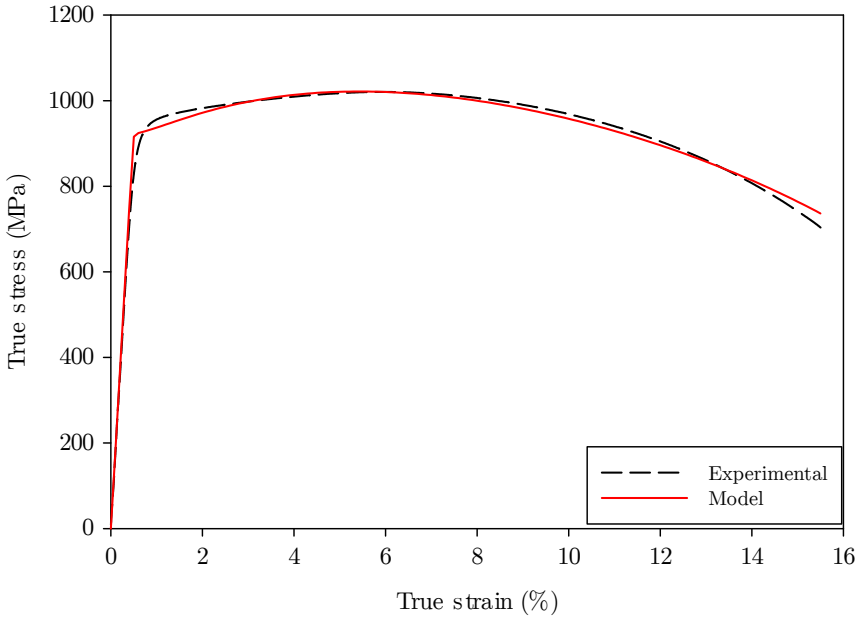

Figure 5: Comparison between the true stress-strain curves of the EN24T steel and the model.

Table 2: Model parameters and descriptions.

Parameter	**Value**	**Unit**
h^s	1.0×10^4	MPa
H^*	3.6×10^{-1}	-
k_D	2.675	- s^{-1}
M	3.1	-
k	1.38×10^{-23}	m^2 kg s^{-2} K^{-1}
T_p	293.15	K
σ^{or}	1.0×10^3	MPa
G	60.15	GPa
b_v	2.4×10^{-10}	m
$\dot{\epsilon}_0''$	1.5×10^{14}	$m^2 s^{-1}$
$Q_{j/v}$	3.0×10^5	J mol^{-1}
R	8.314	J mol^{-1} K^{-1}
β	2.5×10^2	-

The evolution of the four state variables can be seen in Figure 6. A common point for all of them is that the evolution only starts at around 1% strain. This

happens since the backstress, dislocation density, and damage depend on the plastic strain, which only kicks off when the material yields. The plastic strain follows a linear trend, while the damage variable has a parabolic relationship, as expected.

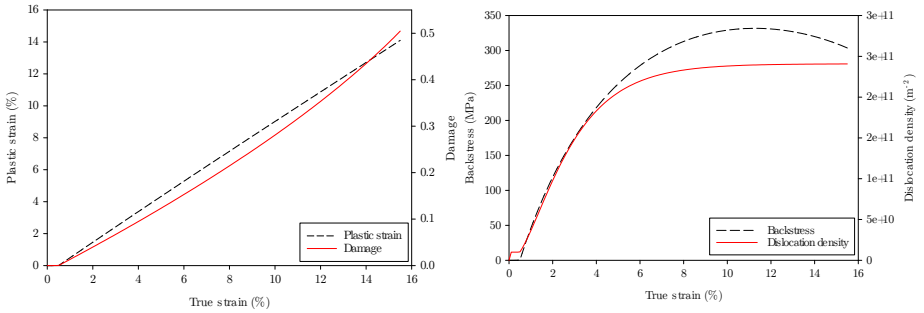

(a) (b)

Figure 6: Evolution of the state variables: plastic strain and damage (a), and backstress and dislocation density (b).

Since the model will be used in a rolling contact fatigue simulation, it is important to understand how the state variables evolve under fatigue. A representative volume element (RVE) consisting of one C3D8R element was then employed in a strain-controlled uniaxial cyclic simulation with three different alternating strains (1.00%, 1.25,% and 1.50%), for 5,000 cycles. The alternating strain shape can be seen in Figure 7. The strain rate was kept the same as in the tensile testing (1.0×10^{-3} s^{-1}), and the R-ratio was equal to zero.

Although the strains chosen for the cyclic simulation are higher than the strains usually observed during wind turbine gears operating in normal conditions, they were chosen due to the fact that this study focuses on simulating severe operating conditions, such as lack of lubrication and misalignments. Such conditions will lead to localised strain concentrations that in turn generate localised damage.

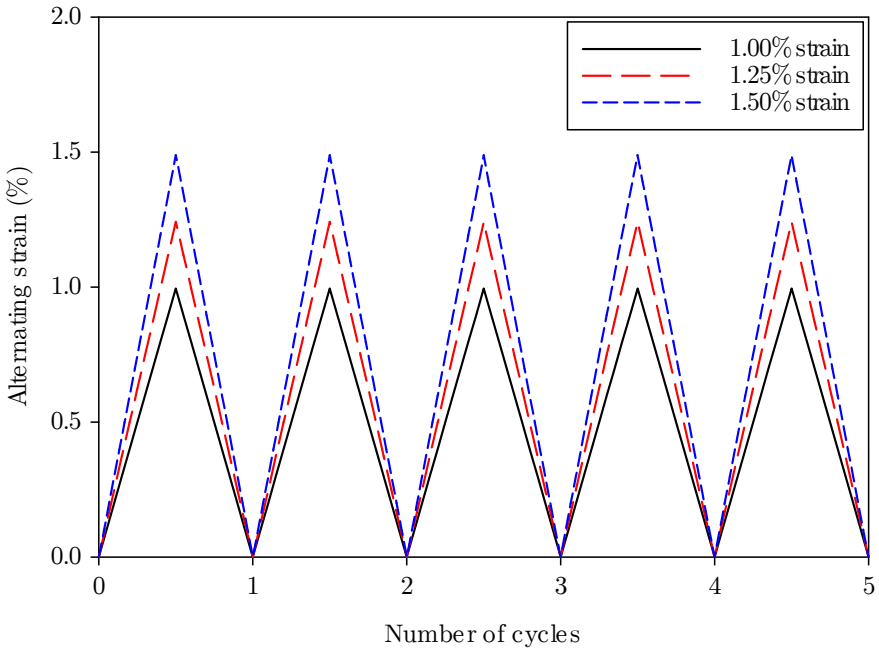

Figure 7: Alternating strain profile versus number of cycles for the strain-controlled cyclic simulations.

Figures 8 and 9 show the state variable evolution for three different maximum strains. All state variables achieve a steady state quickly, showing that the effect of cyclic loading decreases with the increase of number of cycles and tends towards saturation. It is also observed that the higher the strain, the faster this saturation is achieved. Finally, the higher the strain, the higher the values for all state variables, due to the fact they are all dependant on the plastic strain. By extrapolating Figure 9b with the use of the Palmgren–Miner rule [29, 30], the number of cycles until failure would be 645,000, 246,000, and 98,000, for 1.00%, 1.25%, and 1.50% strains respectively.

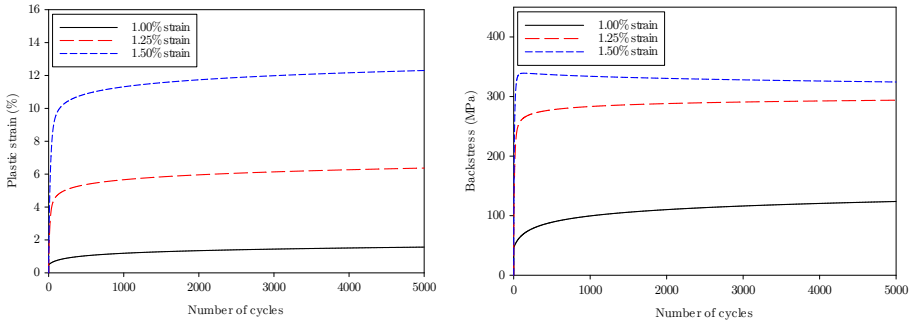

(a) (b)

Figure 8: Evolution of the state variables: plastic strain (a), and backstress (b), in a cyclic strain-controlled simulation with R-ratio = 0.

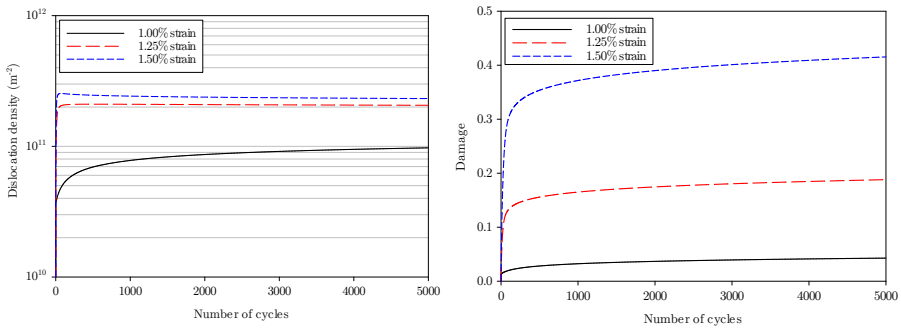

(a) (b)

Figure 9: Evolution of the state variables: dislocation density (a), and damage (b), in a cyclic strain-controlled simulation with R-ratio = 0.

3. Numerical results

A wind turbine is often subjected to varying loads and wind gusts, which might change its operating conditions and generate overloading, lack of lubrication, or misalignments. In this sections, these different service conditions were simulated using the BlueBEAR supercomputer at the University of Birmingham.

Due to the complexity and computational cost of modelling contact fatigue, only a small number of cycles for each operating condition was modelled. This approach is sufficient to show the effectiveness of the model, since as shown in section 2.4, the dislocation accumulation happens very quickly during loading cycles and hence most of the damage is accumulated at early stages.

3.1. Overloading

The finite element model was tested for three different torque values, 100, 150, and 200 N m. The gear pair was perfectly aligned and a coefficient of friction of 0.05 was used. Figure 10 shows the Von Mises stress and damage contours obtained during the simulations. As expected, a higher torque value leads to higher contact and bending stresses. Consequently, the damage for the 200 N m simulation is higher, being barely noticeable on the 150 N m simulation and insignificant on the 100 N m simulation. As the location of the tensile stresses are always changing as the gears turn, the damage and dislocation density move with it, creating the shape that resembles that of a micropit or subsurface cracks.

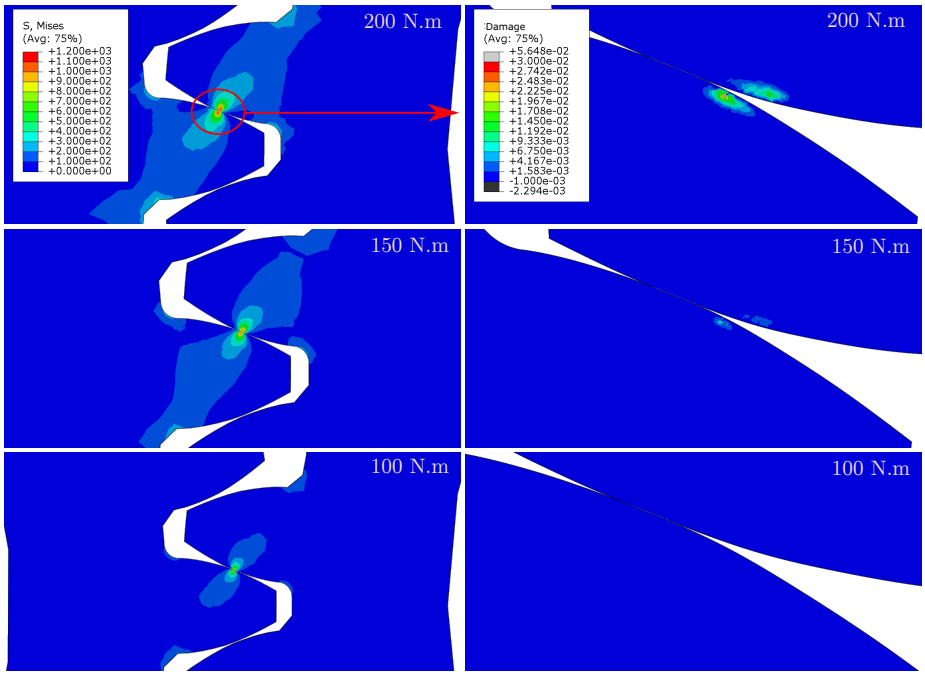

Figure 10: Von Mises (MPa) and damage contour plots after 10 turns, for three different torque values.

Figure 11 shows the damage evolution against the number of cycles. A step-like evolution is identified, where each step is the time where the selected tooth makes contact with the other gear. In every cycle, stress is transferred in between the gear teeth. Plastic strain, and, consequently, damage, is accumulated. Moreover, similarly to the strain-controlled cyclic simulation, the damage is evolving towards a steady state behaviour.

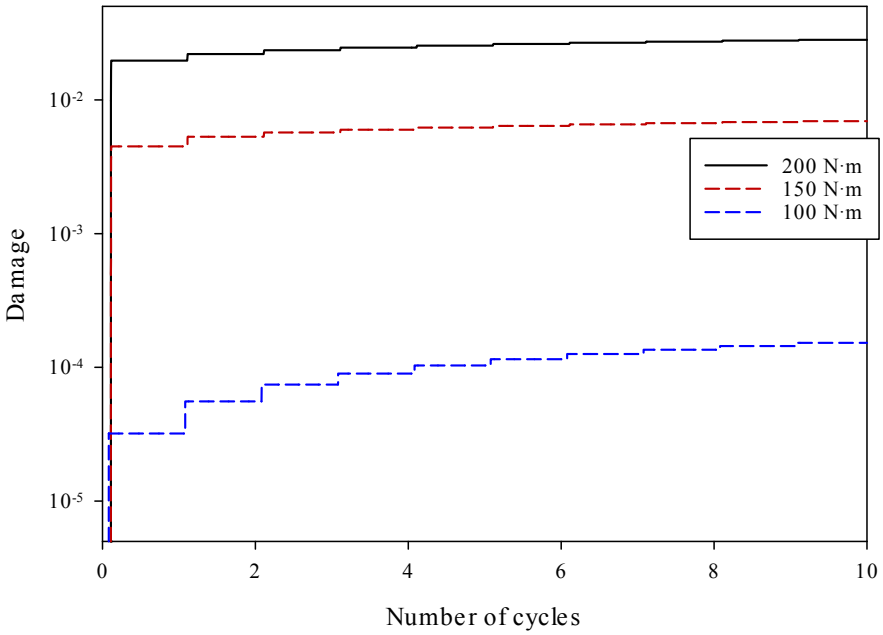

Figure 11: Evolution of the damage variable for three different torque conditions.

3.2. Lubrication

Due to overloading or instant misalignment events, the oil lubricating the gears may be squeezed away, leading to an alternation between dry and lubricated periods. Rebbechi et al. [24] found the coefficient of friction of lubricated gears is usually in the range of 0.04 and 0.06. The coefficient of friction for dry steel on steel contact, on the other hand, is around 0.70 [25, 26]. In addition, if any debris are present, the coefficient of friction can increase even further [27]. In this section, two simulations were run, namely "lubricated" and "dry" simulations. Their coefficients of friction chosen were 0.05 and 0.75, respectively. A torque of 10 N m was applied in each case, during 5 cycles.

Figure 12 shows the Von Mises stress contour plots for both simulations. With the increase of the coefficient of friction, the location of the highest stress moves from the subsurface towards the contact surface, as demonstrated by

Hamilton in ref. [28]. With a higher coefficient of friction, the friction forces increase, thus increasing the contact stress as well. Higher contact stresses may generate plastic deformation, micropitting, and scuffing.

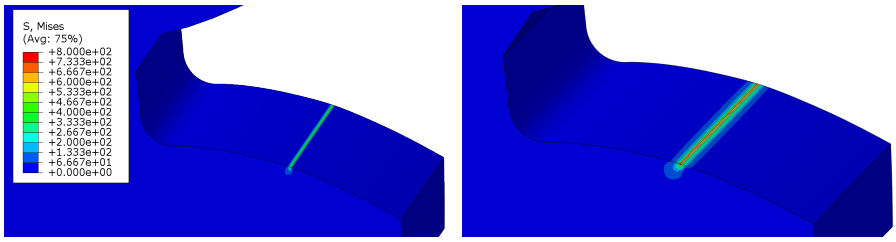

(a) (b)

Figure 12: Von Mises stress (MPa)contour plot for the highest stress obtained during the lubricated (a), and dry (b) simulations.

Due to the lower torque applied (10 N m, in comparison to the 200 N m applied in the overloading simulations), the damage values are expected to be lower. A comparison between the lubricated and dry simulations is shown in Figure 13. The damage variable is 10 orders of magnitude higher in the dry simulation. This shows the oscillation in between dry and lubricated regimes can be quite detrimental and severely reduce WTG life.

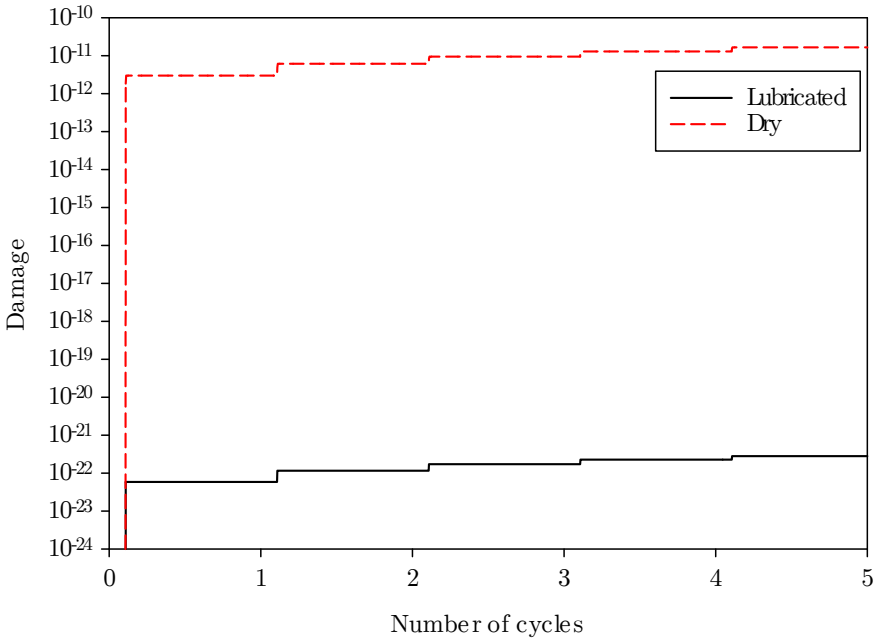

Figure 13: Evolution of the damage variable for the lubricated and dry simulations.

3.3. Misalignments

Different types of misalignment can occur in a gearbox, such as parallel, radial, and angular. Examples of these are shown in Figures 14 to 16. The misalignments were exaggerated in order to aid visualisation.

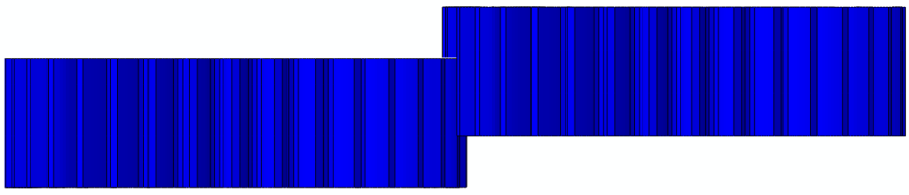

Figure 14: Gear pair in parallel misalignment, top view.

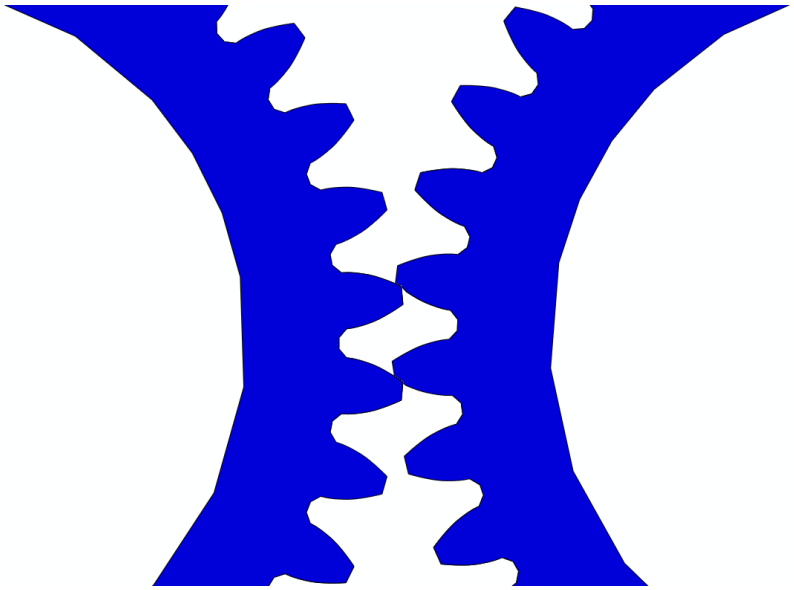

Figure 15: Gear pair in radial misalignment, lateral view.

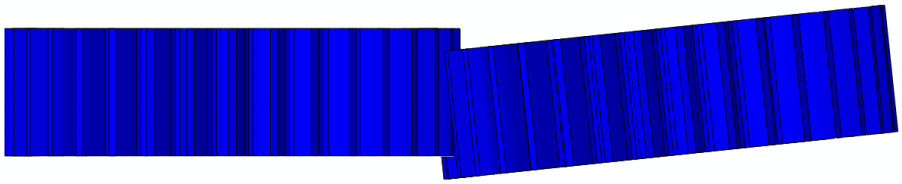

Figure 16: Gear pair in angular misalignment, top view.

The parallel misalignment was generated by translating one of the gears along its z-axis by 40% of its face width. The radial misalignment was produced by translating one of the gears along the x-axis by 40% of its tooth height. Finally, the angular misalignment was obtained by generating by rotating one of the gears along its y-axis by 0.5°. In all simulations, a torque of 10 N m and a coefficient of friction of 0.05 were used.

The Von Mises stress the three types of misalignments are shown in Figures 17 to 19.

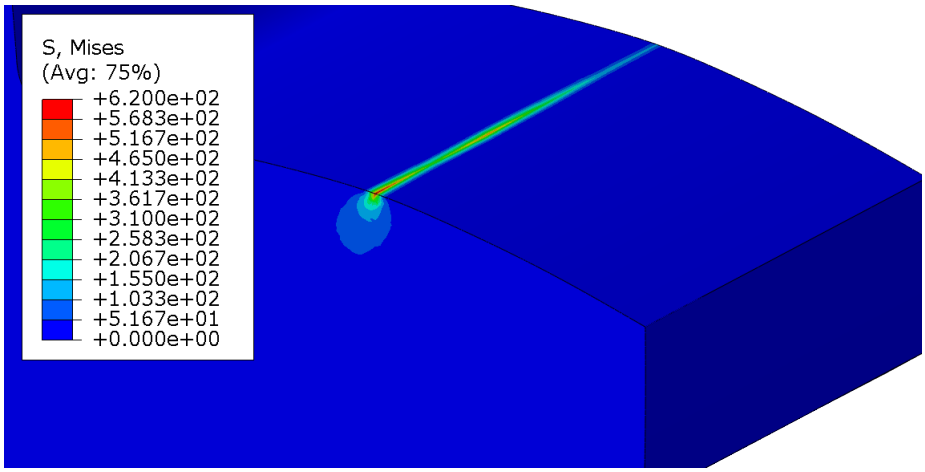

Figure 17: Von Mises stress (MPa) contour plot for the gear with 40% parallel misalignment.

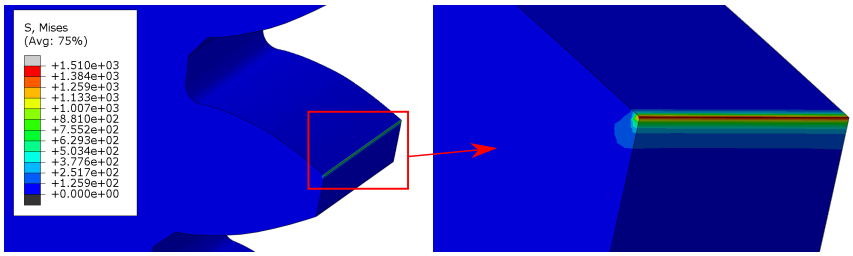

Figure 18: Von Mises stress contour plot for the 40% radial misalignment simulation.

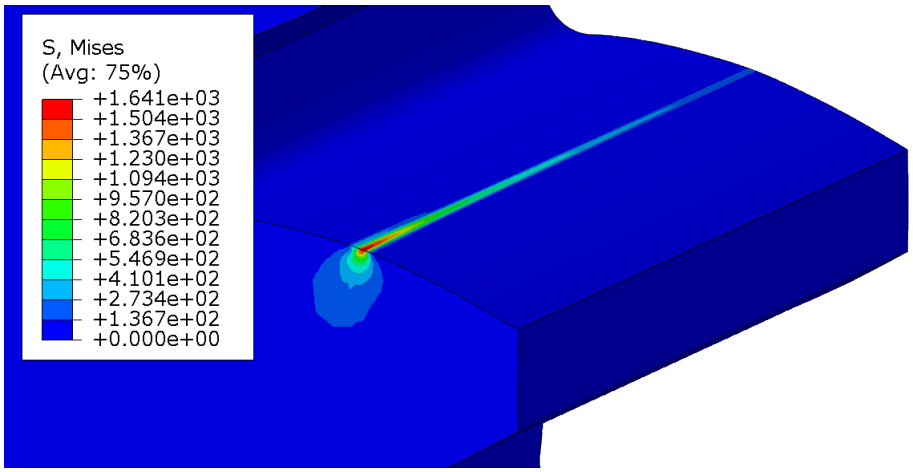

Figure 19: Von Mises stress (MPa) contour plot for 0.5° angular misalignment.

In the parallel misalignment case, it is possible to see that the stress distribution is not uniform along the tooth width. The highest stress concentrations occur at the edge of the tooth flank. A similar contour for the highest stresses is seen on the angular misalignment case. However, the stress values are more than double. For the case of radial misalignment, the highest stresses are localised at the tooth tip. Even though there is a tip relief of 250 µm, the pitch lines of the gears are not in contact as they should be. The involute profile of the gears is manufactured so that the velocity of the gears is constant, avoiding accelerations and decelerations. The misalignment causes the involute profiles of the gears to engage earlier than they should, generating stress concentrations which could lead to damage.

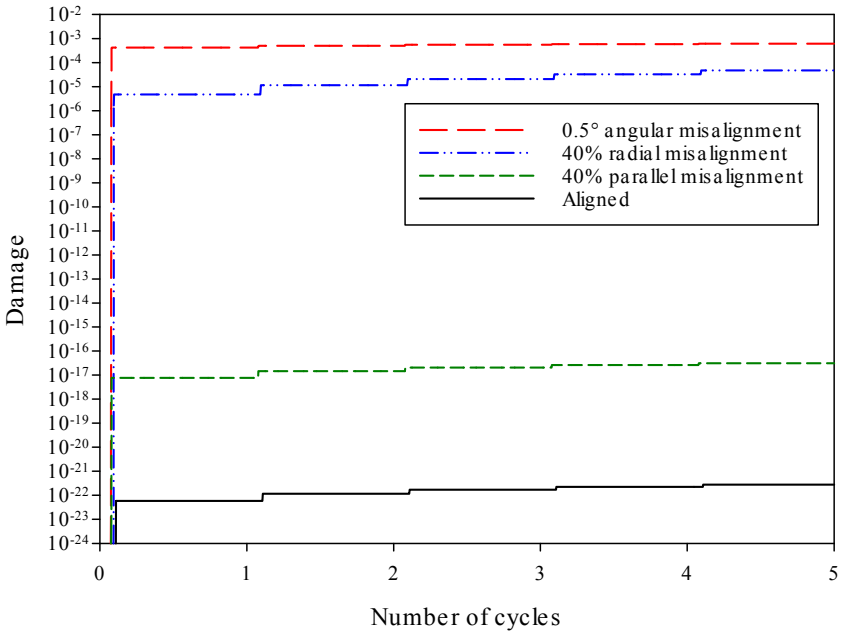

Figure 20: Evolution of the damage variable for the aligned and misaligned simulations.

The results for the damage variable over 5 cycles are shown in Figure 20. An aligned simulation was run for comparison. There is an increase of 5 orders of magnitude for the parallel misaligned simulation, showing that this type of misalignment is not as detrimental as poor lubrication. A bigger difference, however, is observed in the radial and angular misalignment cases. The difference between an aligned gear and a gear with 40% radial misalignment is 17 orders of magnitude. This is even higher for the gear with 0.5° of angular misalignment, where the damage variable increases by 19 orders of magnitude. It is also noteworthy that the torque values for this simulations are only 10 N m. Under normal service conditions, this torque would be higher, and even an instantaneous misalignment, caused by a wind gust, would severely increase damage and reduce the remaining useful lifetime of the component.

4. Discussion

Most WTG maintenance carried out nowadays is corrective or preventive. There is a great effort from the industry in moving towards a more condition-based approach, with the use of vibration analysis, oil monitoring and acoustic emission monitoring, for example.

Due to the highly varying loads to which they are subjected to, being able to predict the damage state of the WTG component is an extremely difficult and complex task. In this section, the data obtained from the service conditions simulations will be used in order to compare and estimate the lifetime of the gear pair used in this study.

Due to the high computational cost, it is impractical to run the previous simulations for more than a handful of cycles. However, it is clear from the previous results that all state variables enter a steady state condition with only a few number of cycles. This means that at every new cycle, the increment on each state variable can be considered as constant.

Therefore, the incremental damage accumulated from the tenth cycle was employed in a Palmgren–Miner rule [29, 30] approach, which assumes a linear damage accumulation. This allows the estimation of the lifetime of the component, and the creation of a stress-cycles (S-N) curve, as shown in Figure 21.

The calculation of Figure 21 was carried out by randomly choosing several integration points at the surface and subsurface of the gear teeth at the fifth cycle. The damage increment of the fifth cycle was then linearly extrapolated until the damage variable reached unit, and the correspondent number of cycles was the expected lifetime of the component.

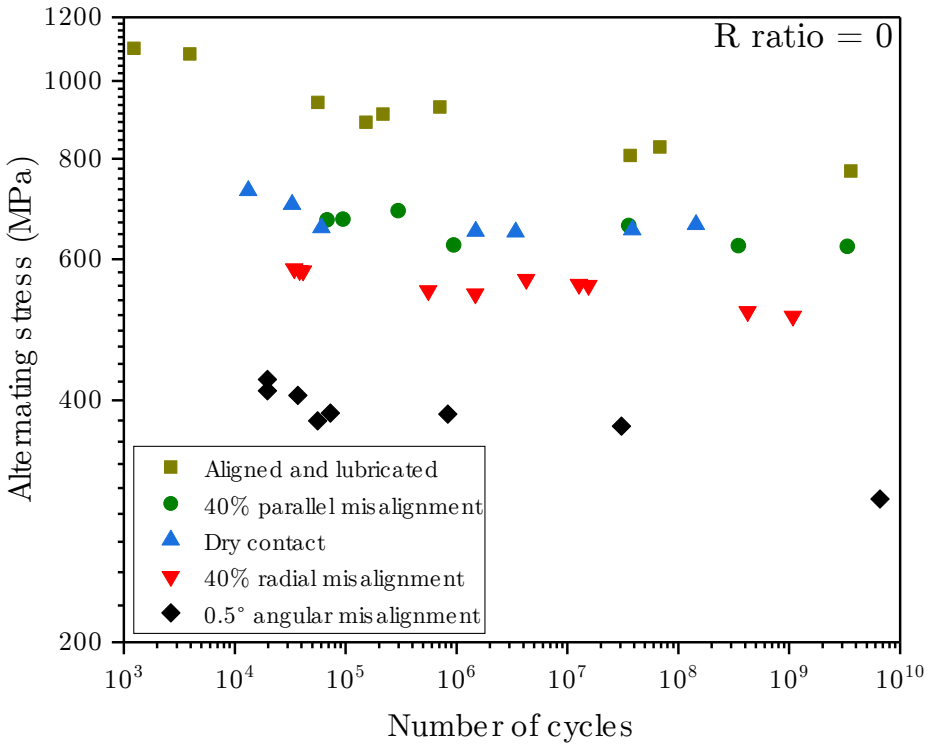

Figure 21: Stress-cycles curve for different service conditions.

From the S-N curve, it becomes clear once again that the angular misalignment is the most detrimental between the tested service conditions, followed by the radial misalignment. The dry contact simulation and the parallel misalignment simulation achieved similar results. The fully lubricated and aligned simulation results are also shown, as a comparison between the other service conditions.

But more than only a comparison of different service conditions, the graph in Figure 21 is an example on how operators can use this model in order to estimate the remaining useful lifetime. For example, if a misalignment event was detected by the vibration monitoring system, the number of cycles of this event can be calculated. With this information, an estimation of the percentage of the useful lifetime that was lost in the event can be made.

For example, 500 cycles of dry contact at 650 MPa would result in a loss of

0.003% of the total useful lifetime. On the other hand, 500 cycles at 400 MPa with a misalignment of only 0.5° reduces the total lifetime by 2.5%! Considering the high speed stage gear rotating at 1500 rpm, it would take minutes for a brand new gear to completely fail. It is noteworthy, however, that this is a conservative estimation, since it is likely that damage will progress at a faster rate at the late stages, diminishing the lifetime even more.

This graph shows the importance of monitoring the wind turbine gearbox service conditions, since even instant misalignment events produced by wind gusts can greatly increase the accumulated damage within the material, and thus reduce the remaining useful lifetime considerably.

5. Conclusions

The following conclusions can be drawn from this study:

1. A constitutive model was developed and calibrated to the EN24T steel. The model was then coupled to a finite element model of a spur gear pair, which presented good correlation to the AGMA equations.
2. The damage evolution depends on the loading and contact conditions. Several service conditions, such as overloading, poor lubrication and misalignments were tested. It was found that the angular misalignment was the most detrimental service condition, followed by radial misalignment, dry contact, and parallel misalignment.
3. Stress-cycles curves based on the simulations and on the constitutive model were then created. They show the model can be used to successfully estimate the remaining useful lifetime of a wind turbine gearbox component. This is a great step towards the implementation of a true predictive maintenance approach.

Acknowledgements

The authors wish to express their appreciation to the National Council of Technological and Scientific Development of Brasil (CNPq) for the financial

support received through the Science Without Borders Scheme.

References

[1] Global Energy Wind Council, Global Wind Report 2018 (2018).

[2] MHI Vestas, MHI Vestas Launches the First 10 MW Wind Turbine in History, http://www.mhivestasoffshore.com/mhi-vestas-launches-the-first-10-mw-wind-turbine-in-history/ (2018).

[3] GE Renewable Energy, An industry first, https://www.ge.com/renewableenergy/wind-energy/turbines/haliade-x-offshore-turbine (2018).

[4] E. Di Lorenzo, G. Kosova, U. Musella, S. Manzato, B. Peeters, F. Marulo, W. Desmet, Structural health monitoring challenges on the 10-MW offshore wind turbine model, Journal of Physics: Conference Series 628 (1) (2015) 12081. doi:10.1088/1742-6596/628/1/012081.

[5] T. Bruce, E. Rounding, H. Long, R. Dwyer-Joyce, Characterisation of white etching crack damage in wind turbine gearbox bearings, Wear 338-339 (2015) 164–167. doi:10.1016/j.wear.2015.06.008.

[6] A. K. Gupta, V. Anirudh, S. K. Singh, Constitutive models to predict flow stress in austenitic stainless steel 316 at elevated temperatures, Materials & Design 43 (2013) 410–418. doi:10.1016/j.matdes.2012.07.008.

[7] H. McQueen, N. Ryan, Constitutive analysis in hot working, Materials Science and Engineering: A 322 (1-2) (2002) 43–63. doi:10.1016/S0921-5093(01)01117-0.

[8] J.-L. Chaboche, Constitutive equations for cyclic plasticity and cyclic viscoplasticity, International journal of plasticity 5 (3) (1989) 247–302.

[9] G. Bernhart, G. Moulinier, O. Brucelle, D. Delagnes, High temperature low cycle fatigue behaviour of a martensitic forging tool steel, International Journal of fatigue 21 (2) (1999) 179–186. doi:10.1016/S0142-1123(98)00064-4.

[10] H. Semba, B. Dyson, M. McLean, Microstructure-based creep modelling of a 9% cr martensitic steel, Materials at High Temperatures 25 (3) (2008) 131–137. doi:10.3184/096034008X354873.

[11] Y. Kadoya, N. Nishimura, B. Dyson, M. McLean, Origins of tertiary creep in high chromium steels, in: 7 th International Conference on Creep and Fracture of Engineering Materials and Structures, 1997, pp. 343–352.

[12] A. S. Pandkar, N. Arakere, G. Subhash, Microstructure-sensitive accumulation of plastic strain due to ratcheting in bearing steels subject to rolling contact fatigue, International Journal of Fatigue 63 (2014) 191–202. doi:10.1016/j.ijfatigue.2014.01.029.

[13] T. Osman, P. Velex, A model for the simulation of the interactions between dynamic tooth loads and contact fatigue in spur gears, Tribology International 46 (1) (2012) 84–96. doi:10.1016/j.triboint.2011.03.024.

[14] M. Franulovic, R. Basan, R. Kunc, I. Prebil, Numerical modeling of life prediction of gears, Procedia Engineering 10 (2011) 562–567. doi:10.1016/j.proeng.2011.04.094.

[15] J. A. Brandão, J. H. Seabra, J. Castro, Surface initiated tooth flank damage: Part I: Numerical model, Wear 268 (1) (2010) 1–12. doi:10.1016/j.wear.2009.06.020.

[16] J. A. Brandão, J. H. Seabra, J. Castro, Surface initiated tooth flank damage. Part II: Prediction of micropitting initiation and mass loss, Wear 268 (1) (2010) 13–22. doi:10.1016/j.wear.2009.07.020.

[17] F. Dunne, N. Petrinic, Introduction to computational plasticity, Oxford University Press on Demand, 2005.

[18] U. Kocks, A. Argon, M. Ashby, Thermodynamics and kinetics of slip, Progress in materials science 19 (1975) 1–281.

[19] H. Basoalto, B. Dyson, Predicting stress relaxation & LCF using a microstructure-based constitutive model, Report, IC Consultants Ltd London (2003).

[20] Y. N. Rabotnov, Creep problems in structural members (1969).

[21] L. Kachanov, Introduction to continuum damage mechanics, Vol. 10, Martinus Nijhoff Publishers, 1986.

[22] ANSI/AGMA 2001-D04, Fundamental rating factors and calculation methods for involute spur and helical gear teeth (2004).

[23] D. S. Simulia, Abaqus 6.13 user's manual, Dassault Systems, Providence, RI (2013).

[24] B. Rebbechi, F. B. Oswald, D. P. Townsend, Measurement of gear tooth dynamic friction, Proceedings of 7th Power Transmission and Gearing (1996) 355–363.

[25] I. S. Grigoriev, E. Z. Meilikhov, A. A. Radzig, Handbook of physical quantities, Vol. 324, CRC Press Boca Raton, 1997.

[26] A. Mussa, P. Krakhmalev, J. Bergström, Sliding wear and fatigue cracking damage mechanisms in reciprocal and unidirectional sliding of high-strength steels in dry contact, Wear 444 (2020) 203119.

[27] I. Sherrington, P. Hayhurst, Simultaneous observation of the evolution of debris density and friction coefficient in dry sliding steel contacts, Wear 249 (3-4) (2001) 182–187.

[28] G. Hamilton, Explicit equations for the stresses beneath a sliding spherical contact, Proceedings of the Institution of Mechanical Engineers, Part C: Journal of Mechanical Engineering Science 197 (1) (1983) 53–59. doi:10.1243/PIME_PROC_1983_197_076_02.

[29] A. Palmgren, Die lebensdauer von kugellargern, Zeitshrift des Vereines Duetsher Ingenieure 68 (4) (1924) 339.

[30] M. Miner, Cumulative damage in fatigue journal of applied mechanics 12 (1945) no. 3, pp, A159-A164 (1945).